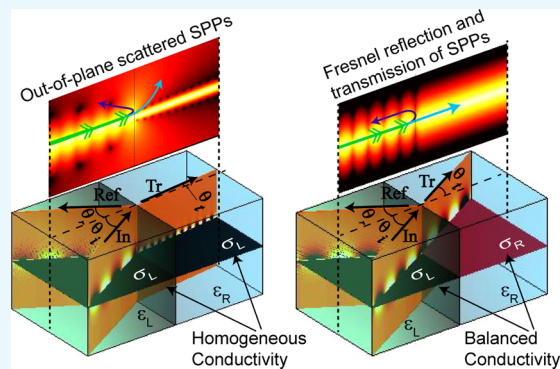


# Fresnel Refraction and Diffraction of Surface Plasmon Polaritons in Two-Dimensional Conducting Sheets

Sandeep Inampudi\* and Hossein Mosallaei\*

Department of Electrical and Computer Engineering, Northeastern University, 100 Forsyth Street, Boston, Massachusetts 02115, United States

**ABSTRACT:** The propagation of surface plasmon polaritons (SPPs) along two-dimensional (2D) materials, such as graphene, is a complex phenomenon linking the microscale electronic properties to macroscale optical properties. Complex geometries increase the complexity of understanding the nature and performance of optoelectronic devices based on surface wave propagation. Here, we demonstrate that under a proper design of macroscopic conductivity profile, the propagation characteristics of SPPs in 2D materials can be made analogous to the propagation of plane waves in homogeneous layers with minimal out-of-plane scattering. Such a direct resemblance enables prediction, design, and calculation of SPP propagation through advanced geometries using fundamental laws of optics. We demonstrate that the propagation of surface waves can be manipulated in-plane using reflection, refraction, diffraction, and also generalized refraction laws analogous to plane waves. We present simple mathematical models to calculate the scattered electromagnetic fields of SPP waves based on Fresnel equations. The presented formulation could facilitate the transfer of many existing plane wave based optical phenomenon to a surface wave based integrated optoelectronic devices.



## 1. INTRODUCTION

The discovery of atomically thin graphene layers<sup>1</sup> followed by other two-dimensional (2D) materials<sup>2</sup> and heterostructures<sup>3</sup> has given a boost to many research areas, including optical and optoelectronic devices.<sup>4,5</sup> Specifically, distinctive interest is in the ability of such materials to support propagation of surface plasmon polaritons (SPPs) in the THz frequency regime with remarkably high confinement factors in comparison to pre-existing metal/dielectric interface systems at visible frequencies.<sup>6</sup> In analogy to metamaterials, physical combinations of these materials have been shown to demonstrate unconventional optical properties, such as hyperbolic dispersion<sup>7,8</sup> and extreme light–matter interactions.<sup>9</sup> The ability to tune the optical properties (surface conductivity and hence the SPP resonance) locally using chemical bonds<sup>10,11</sup> and dynamically using external stimuli, such as gate bias<sup>12</sup> and high magnetic fields,<sup>13</sup> is an additional valuable asset.

The above-mentioned advantages of 2D materials have resulted in various physical phenomena<sup>8,14,15</sup> and efficient devices.<sup>16,17</sup> Whereas most of the structures are based on homogenized patterned surfaces or stacking of layers on top of each other (bilayers and multilayers), it is also important to understand the optical interactions of 2D materials stitched side-by-side with identical or nonidentical optical properties. Fabrication and electronic properties of such designs have been recently demonstrated.<sup>18</sup>

Refraction properties of SPPs, associated with metal/dielectric interfaces previously studied,<sup>19</sup> have demonstrated that a proper choice of metals and dielectrics could eliminate

the out-of-plane scattering of SPPs, restricting their propagation to a 2D plane analogous to plane waves. However, the proper choice requires the permittivities of two out of four metal and dielectric components involved in the system to be uniaxial with three subcriteria to be satisfied. The limited availability in the choice of conventional metals and dielectrics limits the feasibility of satisfying the three subcriteria.

In this work, we focus on predicting and designing the nature of SPP propagation through in-plane stitched 2D materials with homogeneous and patterned intersections. In contrast to conventional metals or dielectrics, 2D materials offer dynamical tunability of their optical properties after the sample fabrication. Utilizing the flexibility of optical properties, we demonstrate that by properly tuning the surface conductivity of the materials in different regions, the SPP propagation can be directly mapped to the fundamental laws of optics, the Fresnel laws, similar to metal/dielectric systems<sup>19</sup> to predict reflection and refraction of surface waves without the requirement of uniaxial nature. In addition, utilizing the flexibility of the physical design of 2D materials, we also demonstrate diffraction and generalized refraction<sup>20</sup> of surface waves at engineered intersections of different media.

Received: October 14, 2016

Accepted: October 24, 2016

Published: November 7, 2016

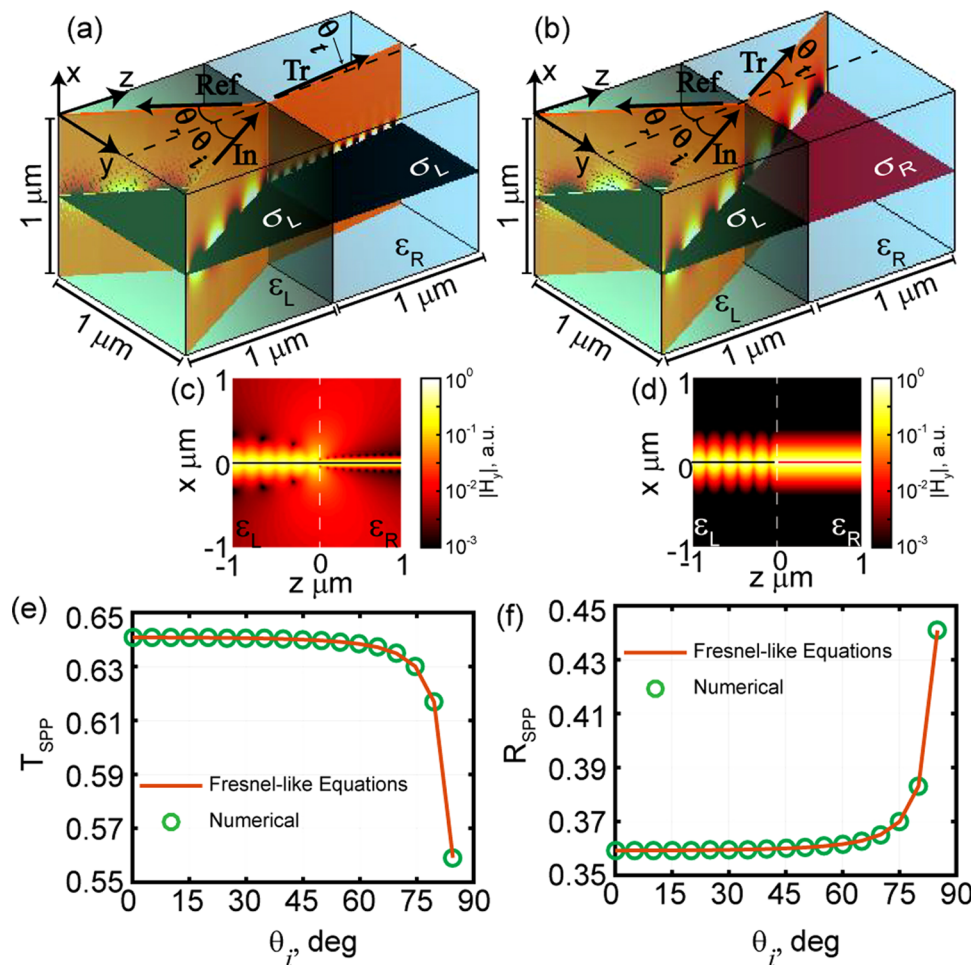


**Figure 1.** SPP reflection and refraction at a homogeneous interface.  $\epsilon_L = 1$  and  $\epsilon_R = 4$ .  $\theta_i$ ,  $\theta_r$ , and  $\theta_t$  represent the incident, reflected, and refracted angles with respect to the normal direction related as  $k_{S,L} \sin \theta_i = k_{S,L} \sin \theta_r = k_{S,R} \sin \theta_t$ ; ( $\theta_i = 30^\circ$ ). (a, c) Calculated real part and magnitude of the in-plane magnetic field component with  $\sigma_L = \sigma_R = \sigma_0$ . (b, d) Calculated real part and magnitude of the in-plane magnetic field component with  $\sigma_L = \sigma_R (\epsilon_L / \epsilon_R) = \sigma_0$ . (e) and (f) are calculated transmission and reflection coefficients of the SPP wave as a function of incident angle for  $\sigma_L = \sigma_R (\epsilon_L / \epsilon_R) = \sigma_0$ , respectively. Solid lines represent eq 9. Symbols represent the values calculated using a numerical method (mode-matching analysis).<sup>28,29</sup> In all cases  $\sigma_0 = 0 + 0.074i$  ( $n_s = 7.3 \times 10^{16} \text{ m}^{-2}$ ) and  $\lambda_0 = 10 \mu\text{m}$ . Losses are removed from the surface conductivity (only in this proof-of-principle results) for clarity in the reflection and transmission values.

## 2. SPP REFLECTION AND REFRACTION

In classical electromagnetics, 2D media (referred to as 2D-sheets hereafter) are considered to be conducting interfaces with strictly zero thickness and nonzero conductivity. The reflection and refraction coefficients of plane-wave electromagnetic fields through homogeneous 2D-sheets with surface conductivity  $\sigma$  separating bulk materials (with relative permittivities  $\epsilon_1$  and  $\epsilon_2$ ) can be derived as

$$\begin{aligned} r^{\text{TE}} &= \frac{k_{x,1} - k_{x,2} - \sigma k_0}{k_{x,1} + k_{x,2} + \sigma k_0}, & t^{\text{TE}} &= \frac{2k_{x,1}}{k_{x,1} + k_{x,2} + \sigma k_0}, \\ r^{\text{TM}} &= \frac{k_0(\epsilon_2 k_{x,1} - \epsilon_1 k_{x,2}) + \sigma k_{x,1} k_{x,2}}{k_0(\epsilon_2 k_{x,1} + \epsilon_1 k_{x,2}) + \sigma k_{x,1} k_{x,2}}, \\ t^{\text{TM}} &= \frac{2k_0 \epsilon_2 k_{x,1}}{k_0(\epsilon_2 k_{x,1} + \epsilon_1 k_{x,2}) + \sigma k_{x,1} k_{x,2}} \end{aligned} \quad (1)$$

where  $\sigma$  is the dimensionless surface conductivity ( $\sigma$ (siemens)/ $\epsilon_0 c$ ),  $k_{x,\{1,2\}}$  represents the wavevector components perpendicular to the 2D-sheet (in the  $yz$ -plane) in each layer.  $k_0$  is the free space wavenumber  $2\pi/\lambda_0$ . TE and TM represent transverse

electric and transverse magnetic polarizations defined with respect to the direction of propagation ( $x$ -axis). When  $\sigma = 0$ , the above equations represent standard Fresnel equations at an interface separating semi-infinite bulk materials with permittivities  $\epsilon_1$  and  $\epsilon_2$ .

SPPs propagate confined to the 2D-sheet with exponentially decaying tails into the bulk layers. The condition for SPP resonance and calculation of its propagation characteristics are studied in ref 14. The reflection and refraction that we discuss in detail in this article correspond to the scattering of surface waves, encountering discontinuities and defects when propagating in-plane ( $yz$ -plane), as shown in Figure 1.

SPPs demonstrate interesting phenomena such as inhomogeneous wave fronts<sup>21</sup> and negative refraction<sup>22</sup> when encountered with such homogeneous defects. The behavior of SPPs at discontinuities and defects is usually unpredictable and often requires complex three-dimensional numerical methods to calculate the scattered electromagnetic fields. Approximate analytic and numerical methods are developed to understand the reflection and out-of-plane scattering of SPP waves at smoothed defects and gaps.<sup>23,24</sup> A transformation optics based approach is also designed to minimize the out-of-plane

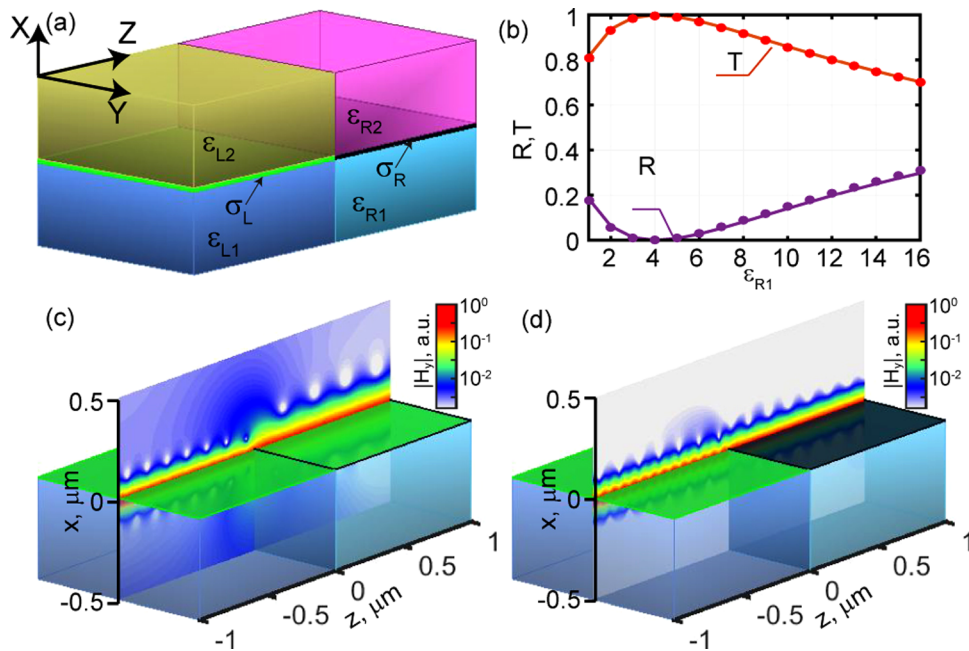


**Figure 2.** (a) Schematic for formulation of Fresnel-like equations for SPP waves. (b) Reflection and transmission coefficients of the SPP wave at normal incidence as a function of  $\epsilon_{R1}$  with  $\epsilon_{L1} = 4$ ,  $\epsilon_{L2} = \epsilon_{R2} = 1$ , and  $\sigma_L = \sigma_R(\epsilon_{L1} + \epsilon_{L2})/(\epsilon_{R1} + \epsilon_{R2}) = \sigma_0$ , where  $\sigma_0 = 0.0008 + 0.074i$  ( $n_s = 7.3 \times 10^{16} \text{ m}^{-2}$ ) and  $\lambda_0 = 10 \mu\text{m}$ . Solid lines represent eq 9. Symbols represent the values calculated using mode-matching analysis.<sup>28,29</sup> (c, d) Calculated magnetic field amplitude of the cross section for  $\epsilon_{L1} = 4$ ,  $\epsilon_{R1} = 2.25$ , and  $\epsilon_{L2} = \epsilon_{R2} = 1$  with eq 11 (c) not satisfied ( $\sigma_L = \sigma_R = \sigma_0$ ) and (d) satisfied ( $\sigma_L = \sigma_R(\epsilon_{L1} + \epsilon_{L2})/(\epsilon_{R1} + \epsilon_{R2}) = \sigma_0$ ).

scattering of SPPs at local defects using anisotropic materials.<sup>25</sup> In realistic devices, such out-of-plane radiation of SPPs is often unwanted. In case of metal/dielectric SPPs, it has been shown that minimization of such parasitic effects requires fabrication of engineered metamaterial structures inside and on top of metal substrates.<sup>19</sup>

In the context of SPPs associated with 2D-sheets, consider a structure as shown in Figure 1a,b, where a 2D-sheet is laterally shared between two dielectric media ( $\epsilon_L$  and  $\epsilon_R$ ). An SPP wave excited from the left side of the left 2D-sheet, not necessarily along the normal direction, encounters a homogeneous intersection with another 2D-sheet and bulk layers at the  $xy$ -plane. At the intersection, it reflects and refracts into surface waves and also scatters out of the plane into free space radiation, as shown in Figure 1c. The reason for the out-of-plane scattering can be attributed to the mismatch in the field decay profiles of the supported SPP waves on the two sides of the interface. By balancing the surface conductivity on each side using the ability to tune the carrier density locally, we demonstrate here that the out-of-plane scattering can be minimized.

The surface conductivity can be locally tuned by varying the carrier density ( $n_s$ ) of the 2D-sheet using gate bias. In the THz frequency regime, the surface conductivity of the graphene layer can be described using the Drude model as

$$\sigma(\omega) = \frac{e^2 \hbar v_f}{\epsilon_0 c \pi \hbar^2} \frac{\sqrt{\pi n_s}}{1/\tau - i\omega} \quad (2)$$

where  $v_f$  represents the Fermi velocity and  $\tau$  represents the relaxation time. The numerical values of the quantities  $v_f = 10^6 \text{ m s}^{-1}$  and  $\tau = 500 \text{ fs}$  are obtained from an experimental work.<sup>26</sup> It has been noted that the quantity  $n_s$  can be varied 2 orders of magnitude from  $10^{16}$  to  $10^{18} \text{ m}^{-2}$ ,<sup>27</sup> which can result in 1 order of magnitude variation in conductivity.

The SPP propagation in each (left and right) half-space individually is characterized by its in-plane wavevector component ( $k_{S,\{L,R\}}$ ), which can be determined by forcing the fields to decay on the two sides of the interface. In fact, for a 2D-sheet with surface conductivity  $\sigma_L$  ( $\sigma_R$ ) in a medium with permittivity  $\epsilon_L$  ( $\epsilon_R$ ) on the left (right) side of the interface, the in-plane SPP resonance wavevector can be analytically expressed as

$$k_{S,\{L,R\}} = k_0 \sqrt{\epsilon_{\{L,R\}} - (2\epsilon_{\{L,R\}}/\sigma_{\{L,R\}})^2} \quad (3)$$

The decay profile of the SPP perpendicular to the sheet is characterized by the perpendicular wavevector component ( $k_{\perp,\{L,R\}}$ ) in each half-space that can be derived using the dispersion relation of the homogeneous layers ( $k_{\perp,\{L,R\}} = \sqrt{k_0^2 \epsilon_{\{L,R\}} - k_{S,\{L,R\}}^2}$ ). An ideal balance between the field decay profiles of the two sides can be obtained when  $k_{\perp,L} = k_{\perp,R}$ , which reduces to the condition

$$\frac{\epsilon_L}{\sigma_L} = \frac{\epsilon_R}{\sigma_R} \quad (4)$$

The balancing condition requires tunability of 2D-sheet conductivity on either side proportional to the ratio of dielectric permittivities of the media they are embedded in. Although monolayer graphene itself has been well known for wide tunable conductivity via doping,<sup>12</sup> considering the atomic scale thickness, multilayered heterostructures can be equivalently used to obtain extreme variations. Recent calculations demonstrate stable forms of heterostructures with abilities to sustain higher doping levels over a broad frequency range.<sup>30</sup> The effect of the surrounding dielectric environment on the surface conductivity has also been investigated.<sup>31</sup>

Note that even though  $\sigma_L$  and  $\sigma_R$  are complex numbers in eq 4, the required ratio  $\sigma_L/\sigma_R$  is real because  $\epsilon_L$  and  $\epsilon_R$  are real (for

dielectrics). The required ratio can be easily managed by changing the carrier density (eq 2), which varies both real and imaginary parts of surface conductivity proportionally.

Figure 1b,d represents the scattering directions and field amplitude, respectively, when the condition in eq 4 is satisfied by the media on two sides. Evidently, the out-of-plane scattering of the SPP is dramatically minimized, as shown in Figure 1d. As an added advantage to the minimization of out-of-plane scattering, the boundary conditions now enable a one-to-one correspondence among the incident, reflected, and refracted SPPs similar to a plane wave incident on a homogeneous interface.<sup>19</sup> This one-to-one correspondence facilitates a direct calculation of amplitudes of the reflected and refracted surface waves using Fresnel-like equations that are derived in detail in the next section for a more generalized system.

### 3. FORMULATION OF FRESNEL-LIKE EQUATIONS FOR SPP PROPAGATION

Consider a geometry as shown in Figure 2a, where space is divided into four quadrants with the left (right) half-space comprising an atomically thin conducting sheet with conductivity  $\sigma_L$  ( $\sigma_R$ ) placed in between two quarter space layers with permittivity  $\epsilon_{L1}$  ( $\epsilon_{R1}$ ) below and  $\epsilon_{L2}$  ( $\epsilon_{R2}$ ) above. The sheets are considered to be in the  $yz$ -plane, and the two (left and right) half-spaces share an interface along the  $xy$ -plane. The normal component of the SPP wavevector along the  $x$ -axis now differs in each quarter space representing the decay of the wave into the bulk layers and can be calculated using the dispersion relation

$$k_{x,mn} = \sqrt{k_0^2 \epsilon_{mn} - k_{S,m}^2} \quad (5)$$

where the square root is solved for a branch cut with a positive imaginary part to satisfy the radiation condition at infinity. The subscript  $m$  represents the quantities in two half-spaces  $m = L, R$ , and the subscript  $n$  represents the quantities in bottom ( $n = 1$ ) and top layers ( $n = 2$ ) of each half-space. As the SPP wave does not necessarily propagate along the normal to the  $xy$ -plane (i.e.,  $k_y \neq 0$ ), the quantity  $k_{S,m}^2$  further decomposes into two components  $k_{S,m}^2 = k_y^2 + k_{z,m}^2$  representing the wavevector components along the  $y$  and  $z$  directions. Note that  $k_y$  is independent of the layer indices since the system is homogeneous in the  $y$  direction,  $k_{z,m}$  is independent of subscript  $n$  because each half-space is homogeneous along the  $z$  direction. The electric and magnetic fields of SPPs in each quarter space can be expressed as<sup>14</sup>

$$\begin{aligned} \vec{\mathcal{E}}_{mn} &= \frac{a_{mn}}{\epsilon_{mn} k_0} \left\{ k_{S,m}, -\frac{k_{x,mn} k_y}{k_{S,m}} p, \frac{k_{x,mn} k_{z,m}}{k_{S,m}} p \right\} e^{i \vec{k}_{mn} \cdot \vec{r}}, \\ \vec{\mathcal{H}}_{mn} &= a_{mn} \left\{ 0, \frac{k_{z,m}}{k_{S,m}}, -\frac{k_y}{k_{S,m}} \right\} e^{i \vec{k}_{mn} \cdot \vec{r}} \end{aligned} \quad (6)$$

The factor  $p$  is equal to  $-1$  and  $+1$  for  $n = 1$  and  $2$ , respectively.  $\vec{k}_{mn}$  is the wavevector, where  $\vec{k}_{mn} = p k_{x,mn} \hat{x} + k_y \hat{y} + k_{z,m} \hat{z}$ . Note that the wavevector components implicitly satisfy the dispersion relation  $k_{x,mn}^2 + k_y^2 + k_{z,m}^2 = k_0^2 \epsilon_{mn}$  in each quarter space. The quantity  $a_{mn}$  represents the amplitude of the decay profile in each quarter space. Forcing the tangential field boundary conditions at the position of the sheet in each half-space individually, one can obtain the relation  $a_{m2}/a_{m1} = 1 + \sigma_m k_{x,m1}/\epsilon_{m1} k_0$ , where  $a_{m1}$  can be arbitrarily chosen to be  $1$ .

Assuming the SPPs solely participate in satisfying the boundary conditions, the tangential boundary conditions at the interface along the  $xy$ -plane can be formulated as

$$\begin{aligned} A_L^+ E_{x,L}^+ + A_L^- E_{x,L}^- &= A_R^+ E_{x,R}^+, \\ A_L^+ H_{y,L}^+ + A_L^- H_{y,L}^- &= A_R^+ H_{y,R}^+ \end{aligned} \quad (7)$$

where from eq 6

$$\begin{aligned} E_{x,\{L,R\}}^\pm &= \mathcal{E}_{x,\{L,R\}n}(\pm k_{z,\{L,R\}}), \\ H_{y,\{L,R\}}^\pm &= \mathcal{H}_{y,\{L,R\}n}(\pm k_{z,\{L,R\}}) \end{aligned} \quad (8)$$

$n = 1$  for  $x < 0$  and  $n = 2$  for  $x > 0$ . The quantity  $A_{\{L,R\}}^\pm$  represents the overall amplitude of the wave envelope propagating in the forward ( $+z$ ) and backward ( $-z$ ) directions.

Solving eq 7, by multiplying the electric field equation with the magnetic field term (vice versa) and integrating over the  $xy$ -plane, the reflection and transmission coefficients of SPP waves defined as  $r_{SPP} = A_L^-/A_L^+$  and  $t_{SPP} = A_R^+/A_L^+$  can be expressed as

$$r_{SPP} = \frac{M_{RL} k_{z,L} - M_{LR} k_{z,R}}{M_{RL} k_{z,L} + M_{LR} k_{z,R}}, \quad t_{SPP} = \frac{2 M_{LL} k_{z,L}}{M_{RL} k_{z,L} + M_{LR} k_{z,R}} \quad (9)$$

where

$$M_{IJ} = \frac{k_{S,I}}{k_{S,J}} \sum_{n=1,2} \left[ \frac{a_{In} a_{Jn}}{\epsilon_{In}(k_{x;In} + k_{x;Jn})} \right] \quad (10)$$

Note that the above equations are similar to the Fresnel equations of plane waves separating two bulk layers.

Firstly, the reflection and transmission coefficients calculated for an intersection, as shown in Figure 1a, employing eq 9 are presented in Figure 1e,f. The calculations of the same quantities performed using accurate numerical simulations (mode-matching method<sup>28,29</sup>) are also presented for comparison. The exact match between the above formulation and numerical calculations demonstrates the validity of the Fresnel-like formulation for SPPs.

Secondly, the formulation can also be applied for a more generalized case where the permittivity of the media in all four quadrants are different. However, the SPP wavevector,  $k_{S,m}$ , in each half-space does not have an exact analytic form when  $\epsilon_{m1} \neq \epsilon_{m2}$ , but can be approximated in the quasistatic limit to the first order as  $k_{S,m} = ik_0(\epsilon_{m1} + \epsilon_{m2})/\sigma_m$ . We verified that the approximation is valid in the entire range of feasible carrier doping concentrations. The approximation transforms the condition for minimizing the out-of-plane scattering to

$$\frac{\epsilon_{L1} + \epsilon_{L2}}{\sigma_L} = \frac{\epsilon_{R1} + \epsilon_{R2}}{\sigma_R} \quad (11)$$

Figure 2b represents the calculated reflection and transmission coefficients of the SPP scattered from an intersection with  $\epsilon_{L1} \neq \epsilon_{L2}$  and  $\epsilon_{R1} \neq \epsilon_{R2}$ . To validate the approximation, reflection and transmission coefficients are calculated using eq 9 as a function of the permittivity of one of the quadrants ( $\epsilon_{R1}$ ). The same quantities are calculated using numerical simulations (mode-matching method<sup>28,29</sup>) for comparison. Figure 2c,d represents the field patterns when eq 11 is not satisfied and satisfied, respectively. An out-of-plane scattering of the SPP can be clearly observed at the intersection in the case of Figure 2c, where a 2D-sheet with identical surface conductivity in both half-spaces ( $\sigma_L = \sigma_R$ ) is shared on different substrates (( $\epsilon_{L1} +$

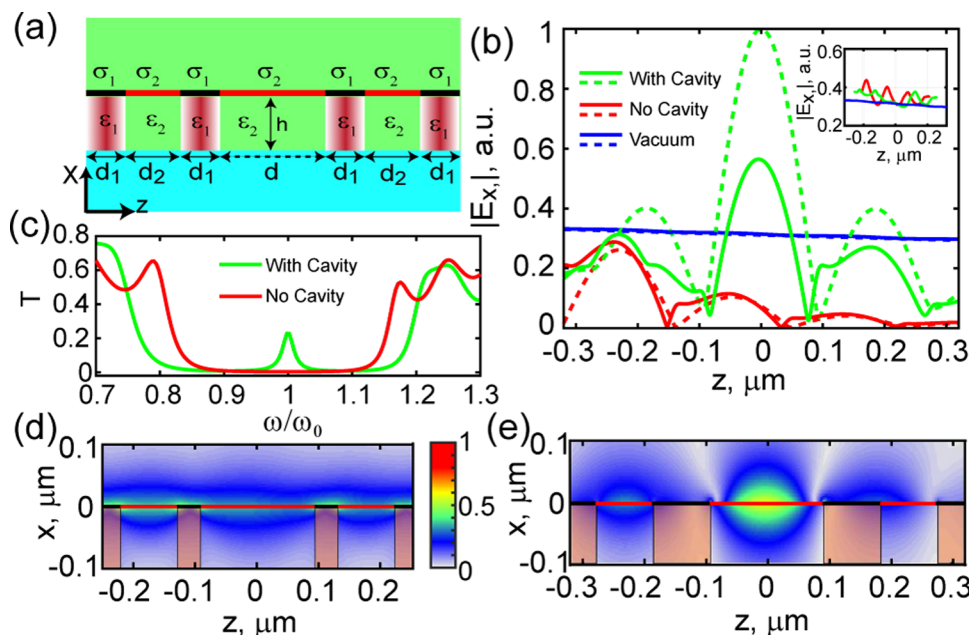


**Figure 3.** (a) Schematic of the plasmonic–photonic crystal design. (b) Amplitude of the normal component of the electric field on top of the 2D-sheet following the criteria in eq 11, “with cavity” implies  $d = 2d_2$ , “no cavity” implies  $d = d_2$ , and “vacuum” implies  $\epsilon_1 = \epsilon_2 = 1$ . The inset represents the same quantities when criteria in eq 11 are not satisfied. (c) The calculated SPP transmission coefficient of plasmonic–photonic crystal representing the frequency ( $\omega$ ) bandwidth of the photonic crystal with and without a cavity, where  $\omega_0 = 2\pi c/\lambda_0$  represents the central frequency. Electric field amplitude along the plasmonic–photonic crystal when the condition in eq 11 is (d) not satisfied and (e) satisfied for the case “with cavity”. In all calculations,  $\epsilon_1 = 4$ ,  $\epsilon_2 = 1$ ,  $\sigma_2 = \sigma_0$ ,  $\sigma_1 = (\epsilon_1 + \epsilon_2)/(2\epsilon_2)\sigma_0$ ,  $d_1 = \lambda_{SPP,1}/4$ ,  $d_2 = \lambda_{SPP,2}/4$ ,  $h = 100$  nm,  $\sigma_0 = 0.0008 + 0.074i$  ( $n_s = 7.4 \times 10^{16} m^{-2}$ ), and  $\lambda_0 = 10 \mu m$ .

$\epsilon_{L2})/\sigma_L \neq (\epsilon_{R1} + \epsilon_{R2})/\sigma_R$ ). A smooth coupling of the SPP with minimum out-of-plane scattering can be observed in the case of Figure 2d, when the surface conductivity on the right-hand side is tuned to satisfy the condition  $((\epsilon_{L1} + \epsilon_{L2})/\sigma_L = (\epsilon_{R1} + \epsilon_{R2})/\sigma_R)$ .

The exact match between the symbols (numerical calculations) and lines (eq 9) demonstrates the validity of the Fresnel-like formulation for the scattering of surface waves at most general intersections. The above can be used to derive an optimized design of optoelectronic devices based on surface waves.

#### 4. PLASMONIC–PHOTONIC CRYSTALS USING 2D-SHEETS

The above-derived Fresnel-like equations can be used to design optoelectronic devices such as SPP-based photonic crystals. Formation of band gaps and field localization regimes in one-dimensional photonic crystals is merely based on reflection and refraction of light at the interfaces and the Bragg periodic condition.<sup>32</sup> Here, we demonstrate that by following the criterion given in eq 11, the photonic crystal phenomenon can also be readily transferred to surface waves on 2D-sheets. A schematic of the plasmonic–photonic crystal is shown in Figure 3a, where a conducting 2D-sheet is placed on a dielectric grating. The surface conductivity of the 2D-sheet is assumed to be tunable locally in the regions of the dielectric and vacuum. Such a design has been experimentally demonstrated as efficient optoelectronic devices to convert electrical signals to optical signals.<sup>17</sup> The thickness of each region is considered to be  $\lambda_{SPP}/4$  and a cavity is introduced in the middle with thickness  $\lambda_{SPP}/2$ . Note that  $\lambda_{SPP}$  is different for different regions.

Accurate electric field amplitudes are calculated for the structures with and without a cavity, and, with and without

following the criterion in eq 11 using the commercial finite element method (FEM) software (COMSOL Multiphysics). The red solid line in Figure 3b represents the normal component electric field amplitude ( $|E_x|$ ) demonstrating prohibition of surface wave propagation in the case of a “no-cavity” (periodic) system when eq 11 is satisfied. When a cavity is introduced into the structure, the electric field is localized inside the cavity region as shown by the green solid line. No such prohibition or localization is seen for the corresponding structures when the criterion in eq 11 is not followed by the surface conductivity profile, as shown in the inset. The dashed lines in Figure 3b represent the field amplitudes calculated for similar structures using the above-derived Fresnel-like formulation. As expected, the Fresnel-like equation overestimates the localization intensity because it disregards the scattering at multiple interfaces. In the case of localization of the field, note that even though the geometry represents a one-dimensional photonic crystal, the SPPs are localized into 2Ds by their nature. The localization area in this example is of the order of  $0.04 \mu m^2$ , where the free space wavelength is  $10 \mu m$ . Figure 3c represents the calculated bandwidth of the SPP photonic crystal. The band gap of the “no-cavity” system is observed to be around 9 THz, and the bandwidth of the field localization “with cavity” is around 1 THz. Figure 3d,e represents the surface plot of the calculated electric field pattern of the structures with a cavity when the criterion in eq 11 is not satisfied and satisfied, respectively.

#### 5. FRESNEL DIFFRACTION OF SPPs

In addition to Fresnel refraction laws, SPPs are also observed to obey diffraction laws similar to plane waves when the media satisfy the criteria in eq 4 or 11. Recent advancements in the fabrication techniques demonstrated the possibility of vertical

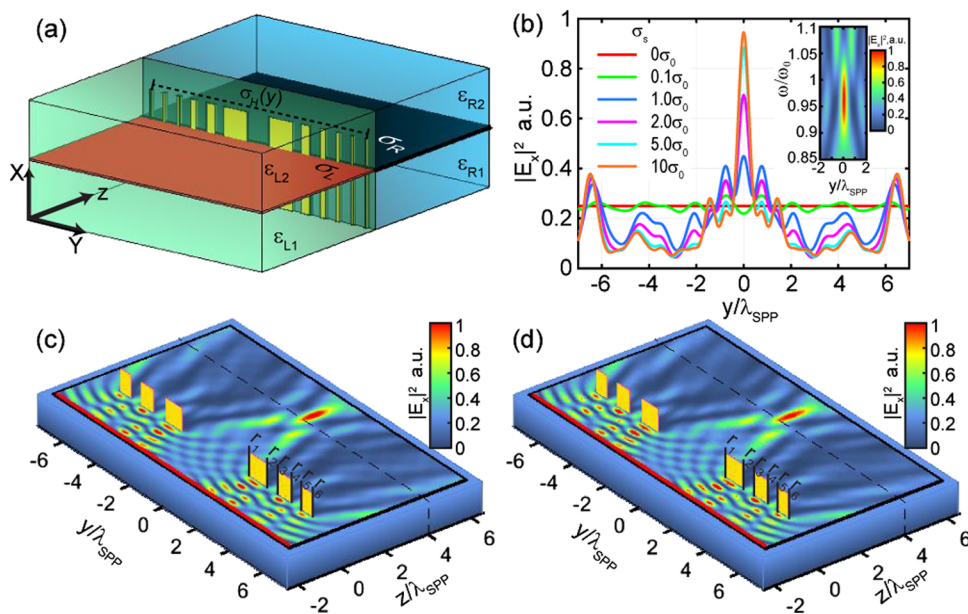


**Figure 4.** (a) Schematic of the in-plane SPP diffraction setup using blocks. (b) Intensity calculated along the focal line ( $f = 4\lambda_{SPP}$ ), demonstrating the evolution of focal spot as a function of conductivity of the block ( $\sigma_s$ ), where  $\sigma_0 = 0.0008 + 0.074i$  ( $n_s = 7.4 \times 10^{16} \text{ m}^{-2}$ ) is the conductivity of the 2D-sheet on the two sides of the blocks. The 2D-sheet is placed on a substrate ( $\epsilon = 2.25$ ) with vacuum on top;  $\lambda_0 = 10 \mu\text{m}$  and  $\lambda_{SPP} \approx 227 \text{ nm}$ . The inset shows the bandwidth of the focal spot as a function of frequency for  $\sigma_s = 10\sigma_0$ . (c) Surface plot of the intensity pattern on the 2D-sheet, demonstrating SPP focusing at the desired focal spot calculated using eq 19 where the conductivity of the blocks  $\sigma_s = 10\sigma_0$ . (d) Intensity pattern calculated using COMSOL for the three-dimensional structure for comparison with a finite block of height and depth equal to 100 nm.

growth of atomic thin materials on substrates.<sup>33–35</sup> The propagation of SPP waves can be controlled in miraculous ways using such perpendicularly grown media when combined with the ability to spatially control the optical properties. One of the popular devices based on Fresnel diffraction are Fresnel zone plates (FZPs), which are designed to focus diffracted plane waves to a desired focal spot. We demonstrate focusing of SPP waves into wavelength-sized diffraction-limited spots at a desired focal distance on the surface of the 2D-sheet following the FZP design.

FZPs are primarily designed as consecutive opaque and transparent ring patterns to focus light at a desired focal distance  $f$ . The design is according to the condition to form constructive interference of the diffracted beams at the focal distance. The radius of the  $l$ th ring to focus light at a distance  $f$  from the pattern is given by the formula

$$r_l = \sqrt{l\lambda f + (\lambda/2)^2} \quad (12)$$

In the context of SPPs associated with 2D-sheets, where the wave resides completely on the surface, the ring pattern can be reduced to perpendicular blocks that block and allow the propagation of SPPs (acting like transparent and opaque screens), as shown in Figure 4a. In contrast to the structures in Figures 1a and 2a, the intersection is now considered inhomogeneous along the  $y$  direction.

The computation of electromagnetic fields of the surface waves through such a three-dimensional system can also be reduced to an analytic model when the condition in eq 11 is satisfied by the media on both sides. The model has been derived on the basis of rigorous coupled wave analysis<sup>36</sup> formalism, which is mainly developed for diffraction gratings with a nonzero thickness. Here, we modify it for the case of a spatially modulated interface (a zero-thickness interface

grating) between two half-spaces with a conductivity profile defined by  $\sigma_H(y)$ .

To do so, we begin with the modification of the boundary condition in eq 7 to include (1) the effective spatially dependent conductivity pattern of the boundary and (2) the diffraction orders of the SPP wave originated due to the pattern. Note that as long as the condition in eq 4 or 11 is satisfied, the vertical decay profiles of all of the waves are identical, forcing all of the diffraction orders to be surface waves traveling in different in-plane directions. The modified boundary conditions for a conductivity pattern of  $\sigma_H(y)$  along the  $y$ -axis can be expressed as

$$\begin{aligned} \sum_{g=-\infty}^{\infty} [A_L^{+(g)} E_{x;L}^{+(g)} + A_L^{-(g)} E_{x;L}^{-(g)}] e^{ik_y^{(g)} y} &= \sum_{g=-\infty}^{\infty} A_R^{+(g)} E_{x;R}^{+(g)} e^{ik_y^{(g)} y}, \\ \sum_{g=-\infty}^{\infty} [A_L^{+(g)} H_{y;L}^{+(g)} + A_L^{-(g)} H_{y;L}^{-(g)}] e^{ik_y^{(g)} y} &= \sum_{g=-\infty}^{\infty} A_R^{+(g)} H_{y;R}^{+(g)} e^{ik_y^{(g)} y} \\ + \sigma_H(y) \sum_{g=-\infty}^{\infty} A_R^{+(g)} E_{x;R}^{+(g)} e^{ik_y^{(g)} y} \end{aligned} \quad (13)$$

where each diffraction order is characterized by its wavevector parallel to the interface  $k_y^{(g)}$ . The exponential function,  $e^{ik_y^{(g)} y}$ , is explicitly shown in the equation factoring out from the field profile terms in eqs 6 and 8 for clarification purposes. The diffraction orders, characterized by the parallel wavevector components, are usually discrete following the Floquet condition  $k_y^{(g)} = k_{y0} + g2\pi/\Lambda$ , where  $\Lambda$  is the periodicity of the pattern and  $k_{y0}$  is the component representing the direction of the incident wave. If  $\sigma_H(y)$  profile is not periodic in  $y$  (as is the case of the FZP condition), then a supercell structure with virtually infinite periodicity ( $\Lambda \rightarrow \infty$ ) can be imagined, transforming the discrete set of  $k_y^{(g)}$  components into a continuous spectrum. Note that as the sheets are assumed to be isotropic, the in-plane wavevector components of all of the

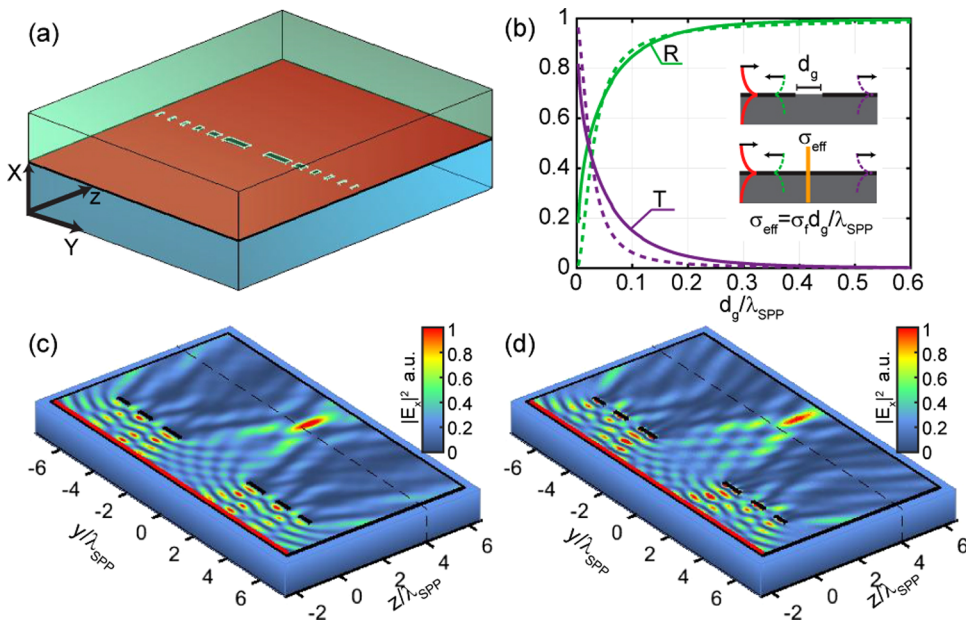


**Figure 5.** (a) Schematic of the in-plane SPP diffraction setup using rectangular holes. (b) Calculated and fit curves of the reflection and transmission coefficients of SPPs as a function of gap width ( $d_g$ ). The inset shows the model for calibration. Surface conductivity on the two sides of the gap is assumed to be  $\sigma_0 = 0 + 0.074i$  for the model. The 2D-sheets are placed on a substrate ( $\epsilon = 2.25$ ) with vacuum on top;  $\lambda_0 = 10 \mu\text{m}$  and  $\lambda_{\text{SPP}} \approx 227 \text{ nm}$ . The extracted fit parameter  $\sigma_f$  in this case is  $0.3791 + 2.7346i$ . (c) Surface plot of the intensity pattern on the 2D-sheet demonstrating SPP focusing at the desired focal spot ( $f = 4\lambda_{\text{SPP}}$ ) calculated using eq 19 for the hole width  $d_g = 30 \text{ nm}$ ,  $\lambda_0 = 10 \mu\text{m}$ , and  $\sigma_0 = 0.0008 + 0.074i$  ( $n_s = 7.4 \times 10^{16} \text{ m}^{-2}$ ) on both sides. (d) The intensity pattern calculated using COMSOL for the three-dimensional structure with actual holes for comparison. The focal spot shifted to a distance of  $\lambda_{\text{SPP}}/2$  due to the additional phase difference of  $(\pi)$  added by the holes.

diffraction orders has to be conserved following the condition  $k_{S,m}^2 = k_y^{(g)^2} + k_{z,m}^{(g)^2}$ .

Expanding the conductivity profile into its Fourier harmonics

$$\sigma_H(y) = \sum_{g'=-\infty}^{\infty} \xi_{g'} e^{ig'2\pi/\lambda y} \quad (14)$$

and by applying convolution to the double sum in the last term of eq 13, the modified boundary condition can be reduced to a matrix form. Utilizing the orthogonality of the exponential basis functions, the boundary condition in the matrix form can be represented as

$$\begin{aligned} E_{x,L}^+ A_L^+ + E_{x,L}^- A_L^- &= E_{x,R}^+ A_R^+, \\ H_{y,L}^+ A_L^+ + H_{y,L}^- A_L^- &= H_{y,R}^+ A_R^+ + \Xi E_{x,R}^+ A_R^+ \end{aligned} \quad (15)$$

where now the quantities  $E_x^\pm$  and  $H_y^\pm$  are diagonal matrices with each element along the diagonal representing the field profile in eq 8 for each diffraction order characterized by  $k_y^{(g)}$ . The matrix  $\Xi$  is the convoluted matrix of Fourier harmonics of the conductivity profile where  $ij$ th element can be expressed as

$$\Xi_{ij} = \xi_{i+j} \quad (16)$$

Multiplying the electric field equation in eq 15 with each magnetic field component and vice versa, the modified boundary conditions can be solved for reflection and transmission coefficient matrices, relating the amplitude vectors of the diffraction orders,  $A_L^- = r_{\text{SPP}} A_L^+$  and  $A_R^+ = t_{\text{SPP}} A_L^+$ , as

$$\begin{aligned} r_{\text{SPP}} &= D^{-1} [k_0(M_{RL} k_{z,L} - M_{LR} k_{z,R}) - N_{LR} \Xi], \\ t_{\text{SPP}} &= D^{-1} [2k_0 M_{LL} k_{z,L}] \end{aligned} \quad (17)$$

where  $M_{IJ}$  has the same definition as in eq 10 and

$$\begin{aligned} D &= k_0(M_{RL} k_{z,L} + M_{LR} k_{z,R}) + N_{LR} \Xi, \\ N_{LR} &= k_{S,L} k_{S,R} \sum_{n=1,2} \left[ \frac{a_{L,n} a_{R,n}}{\epsilon_{L,n} \epsilon_{R,n} (k_{x,L,n} + k_{x,R,n})} \right] \end{aligned} \quad (18)$$

$k_{z,L}$  and  $k_{z,R}$  are diagonal matrices where the elements are  $k_z^{(g)}$  values of each diffraction order. The total electric and magnetic field components can be expressed as a sum of the field components of all diffraction orders as

$$\begin{aligned} E_x(\vec{r}) &= \sum_{g=-\infty}^{\infty} [A_I^{+(g)} E_{x,I}^{+(g)} + A_I^{-(g)} E_{x,I}^{-(g)}] e^{ik^{(g)} \cdot (\vec{r})}, \\ H_y(\vec{r}) &= \sum_{g=-\infty}^{\infty} [A_I^{+(g)} H_{y,I}^{+(g)} + A_I^{-(g)} H_{y,I}^{-(g)}] e^{ik^{(g)} \cdot (\vec{r})} \end{aligned} \quad (19)$$

where  $I$  represents L,R depending on the location of  $\vec{r}$ . Notice that when the interface between the two spaces has a homogeneous conductivity profile (i.e.,  $\sigma_H(y) = \text{const}$ ), the SPP does not scatter into diffraction orders, which reduces the matrices in eq 17 to singleton elements. A similarity in eqs 17 and 1 can be seen in such a case, representing an analogy between the scattering of a plane wave at a conducting interface and the scattering of a SPP wave at a conducting interface perpendicular to the direction of propagation.

To demonstrate focusing of SPP waves using FZP, three rings (six blocks) are considered perpendicular to the 2D-sheet, as shown in Figure 4c. The pattern is symmetric with respect to the  $xz$ -plane. On each side, the radius in eq 12 defines the position of transition from the transparent (gap) to the opaque (block) region. Hence, the position (of the nearest corner to the center) of each block is given by  $r_1, r_3$ , and  $r_5$  and the lateral width of each block is given by  $r_2 - r_1, r_4 - r_3$ , and  $r_6 - r_5$ ,

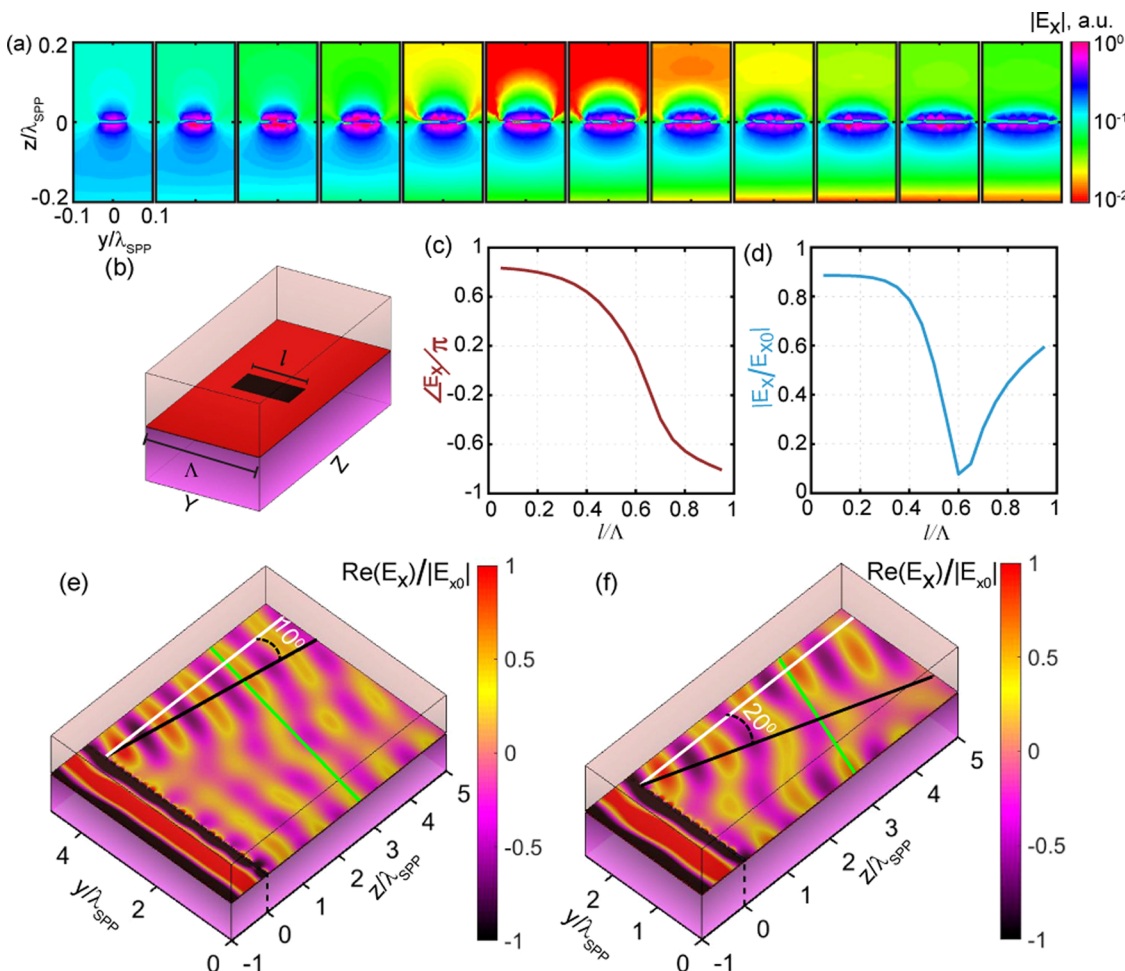


**Figure 6.** Generalized refraction of SPPs on the 2D-sheet using phase gradient of in-plane hole antennae. (a) Calculated amplitude of the electric field normal component using COMSOL for the unit cell shown in (b) for hole widths ranging from  $l = 0.35$  to  $0.90 \Lambda$ . Resonant behavior is observed at  $l = 0.60 \Lambda$ . The slit width is 5 nm. Calculated phase (c) and amplitude (d) of the SPP wave transmitted through the hole antennae as a function of hole width  $l$ . (e) and (f) represent the calculated normal component of the electric field normalized to the incident field for “metoline” defects with hole antennae arranged for  $\theta_0 = 10$  and  $20^\circ$ , respectively. White, black, and green solid lines in (e) and (f) represent the normal, propagation, and wavefront directions, respectively. In all calculations,  $\lambda_0 = 10 \mu\text{m}$ ,  $\sigma_0 = 0.0008 + 0.074i$  ( $n_s = 7.4 \times 10^{16} \text{ m}^{-2}$ ) and  $\epsilon_{\text{sub}} = 2.25$ .

respectively. In Figure 4c, the geometry is designed to focus the SPP wave at  $f = 4\lambda_{\text{SPP}}$ . The vertical component of the electric field on top of the 2D-sheet at the focal line is calculated using eq 19. Figure 4b represents the evolution of the focal spot as a function of the surface conductivity of the blocks. As expected, as the surface conductivity of the blocks increases, the SPP wave gets tightly focused on the plane of the 2D-sheet. The size (full-width at half-maximum) of the focal spot is found to be equal to the width of the last (third) ring, which is one of the properties of the FZPs. The size of the focal spot can be minimized by adding more rings. The inset of Figure 4b represents the bandwidth of the focal spot. For the same geometry, the field along the focal plane is calculated by varying the frequency of the incident light. The focal spot appears for a reasonable bandwidth range (around 5 THz). Figure 4c represents the surface plot of the intensity pattern overlapped on the structure demonstrating a tight focus near the focal spot.

The primary difference between the actual three-dimensional structure and the assumed design in the above formalism is the height of the blocks (assumed to be infinite). The assumption is valid as long as the height (and depth) of the blocks is greater than the SPP decay length. To validate the above formulation, numerical simulations are performed on the actual three-

dimensional structure using the FEM software (COMSOL Multiphysics), where the height and depth of the blocks are considered to be finite (100 nm each). An SPP wave is excited on the  $xy$ -plane along the red solid line shown in Figure 4d. The calculated intensity demonstrates a pattern identical to that in Figure 4c, validating both the concept of focusing SPP waves using the FZP condition and the described analytic approach. Note that the media in left and right half-spaces are considered identical in this example; however, the principle works as long as the condition in eq 11 is satisfied.

The same phenomenon can also be observed using a complementary structure where the screens are replaced with holes in the 2D-sheet with the same lateral dimension. The focusing efficiency in the case of FZP primarily depends on the opacity and transparency of the rings of the pattern. As the SPPs on 2D-sheets are known to reflect from the discontinuities in the 2D-sheets, a screen can be realized just by drilling a rectangular hole into the 2D-sheet. We observe that gaps of width 30 nm ( $\approx \lambda_{\text{SPP}}/7.5$ ) nearly reflect back 80% of the SPP wave, enough to demonstrate the focusing principle using the FZP condition.

A schematic of the hole design is shown in Figure 5a, where holes are drilled in a homogeneous 2D-sheet. In practice, zero

surface conductivity locally in a regime can also be achieved by chemical bonds.<sup>11</sup> Utilizing eq 17 to calculate the electromagnetic fields is not a straightforward process in the case of holes. A rectangular hole (slit or gap) in a homogeneous 2D-sheet reflects and refracts SPP waves acting like a perpendicular conducting interface similar to that in Figure 4. To approximate it as an interface between two half-spaces, the effective surface conductivity of the hole pattern needs to be calculated. Here, we calibrate the “hole” conductivity pattern by calculating the reflection and transmission coefficients through it and using a numerical fitting method. The model we assume for the fitting process is shown in the inset of Figure 5b. We assume that the effective conductivity of the hole ( $\sigma_{\text{eff}}$ ) is linearly proportional to the gap size ( $\sigma_{\text{eff}} = \sigma_f d_g / \lambda_{\text{SPP}}$ ), where  $\sigma_f$  is the fit parameter and  $d_g$  is the gap width. The actual reflection and transmission coefficients of the SPP are calculated using the mode-matching analysis<sup>28,29</sup> and has been fit to eq 17 to calculate  $\sigma_f$ . The calculated reflection and transmission coefficients along with the fit curves are shown in Figure 5b. Note that the model is valid to approximate the absolute value of the reflection and transmission coefficients but not the phase because the thickness of the gap is ignored.

Once the effective conductivity of the hole is calibrated, eq 17 can safely be applied to the hole system. Figure 5c represents the intensity pattern through a hole system where the lateral dimensions of the holes are designed according to eq 12 and the width along the  $z$ -axis is considered to be  $d_g = 30$  nm  $\approx 0.13\lambda_{\text{SPP}}$ . SPP waves focus at the target line as expected. The actual three-dimensional structure with holes is simulated using COMSOL and is presented in Figure 5d for comparison with the same excitation process as in Figure 4d. A shift in the focal spot position (exactly equal to  $\lambda_{\text{SPP}}/2$ ) is observed in the COMSOL simulations with an actual three-dimensional structure due to an additional ( $\pi$ ) phase difference added by the holes.

## 6. GENERALIZED REFRACTION OF SPPs

In this section, we demonstrate manipulation of SPP propagation confined to the 2D-sheet using the recent innovative modification of the Fresnel equations known as the generalized law of refraction.<sup>20,37</sup> It has been demonstrated that the refraction of plane waves can be deviated from the fundamental Fresnel refraction angle by adding an engineered phase gradient to the refracting interface; the emerging area of metasurfaces.<sup>38–42</sup> The required phase gradients have been obtained by patterning the surfaces with various types of resonating elements of subwavelength dimensions.<sup>43,44</sup>

Analogously, resonating elements can be implanted on the 2D-sheets to manipulate the propagation of SPPs. We demonstrate that the resonating element here can be as simple as a line of rectangular holes drilled into the 2D-sheet with subwavelength dimensions.<sup>45,46</sup> The physical dimension of the holes being zero in the direction perpendicular to the 2D-sheet, we call them “metalines”; drawn on top of the 2D-sheet to manipulate the surface wave.

The resonance characteristics of in-plane periodic hole antennae in response to SPP excitation are presented in Figure 6a,c,d. The unit cell considered for the characterization is shown in Figure 6b. The in-plane hole antennae are considered with fixed width (5 nm in the direction of SPP propagation along the  $z$ -axis). The periodicity ( $\Lambda$ ) of the unit cell is considered to be  $\lambda_{\text{SPP}}/5$ . The amplitude and phase of the scattered (SPP) wavefront are calculated using the FEM

software (COMSOL Multiphysics) by varying the length of the hole from 0.05 to 0.95  $\Lambda$ . Figure 6a represents the magnitudes of the electric field normal components scattered through the holes in the range between 0.35 and 0.90  $\Lambda$ , demonstrating excitation of resonant gap modes around 0.6  $\Lambda$ .<sup>47</sup>

The corresponding phase and amplitudes are presented in Figure 6b, where due to the resonance a phase gradient nearly ranging between  $-0.8\pi$  and  $+0.8\pi$  is observed. The amplitude of the transmitted field is not uniform, which hinders the performance of the wavefront. More variations in the shape of the hole can be considered to have uniform transmittance; however, here we aim at demonstrating the proof of concept with a simple geometry.

The capabilities of the hole antennae to bend the SPP wave in-plane has been demonstrated in Figure 6c,d. The holes are drilled in the 2D-sheet along a line with a uniform center-to-center spacing of  $\Lambda$ . The length of each hole is chosen to have a uniform phase gradient from right to left ( $-y$  direction), and the number of holes is chosen to cover the full available phase range. The phase gradient required to bend the wavefront to an angle  $\theta_b$  is calculated as

$$d\phi = 2\pi \frac{\Lambda}{\lambda_{\text{SPP}}} \sin \theta_b \quad (20)$$

FEM (COMSOL) simulations are performed using SPP excitation on the unit cells designed according to the above description aiming at a bending angle of 10 and 20°. The resultant field patterns demonstrating the wavefront bending to expected angles are presented in Figure 6e,f, respectively. The solid lines in Figure 6e,f represent the normal to the defect line (white), the direction of propagation (black), and wavefront (green) of the surface waves. The nonuniformity of the resultant wavefront is due to the lower transmission amplitudes of the holes in some regions. The bending of wavefronts to expected angles demonstrates that SPP can be manipulated using the generalized Fresnel law similar to plane waves.

In conclusion, we demonstrated that on proper design of the conductivity profile of 2D materials, the out-of-plane scattering of SPP waves can be dramatically minimized at abrupt intersections. In such a design, the propagation characteristics of SPPs resemble the propagation characteristics of plane waves, enabling the engineering of complex optoelectronic devices using fundamental laws of optics. Utilizing the above resemblance, we demonstrated designs of plasmonic–photonic crystals to localize the surface wave into deep subwavelength volumes. In addition, under the same criteria, SPPs also obey the diffraction laws identical to plane-wave diffraction, facilitating more methods to control the SPP propagation in the plane of the material. We demonstrated focusing of SPPs using FZPs, a device primarily designed for plane waves. In addition, under the same criteria, SPPs are also observed to obey the generalized Fresnel refraction laws. A design based on line defects (metoline) is presented to manipulate the propagation of SPP waves in the plane of the 2D-sheets based on the generalized law of refraction, giving a finer control on engineering the SPP propagation on the 2D-sheets. Whereas we illustrated the proof of concept with a few examples, many existing laws of plane-wave optics can be transferred to SPP waves using the proposed criteria and mathematical formulation.

## AUTHOR INFORMATION

### Corresponding Authors

\*E-mail: [n.inampudi@neu.edu](mailto:n.inampudi@neu.edu) (S.I.).  
\*E-mail: [hosseinnm@coe.neu.edu](mailto:hosseinnm@coe.neu.edu) (H.M.).

### Notes

The authors declare no competing financial interest.

## ACKNOWLEDGMENTS

This work is supported by the ARO MURI award grant W911NF-14-0247. The authors gratefully acknowledge Prof. E. Kaxiras and S. N. Shirodkar (Department of Physics, Harvard University) for useful discussions and comments.

## REFERENCES

- (1) Novoselov, K. S.; Geim, A. K.; Morozov, S. V.; Jiang, D.; Zhang, Y.; Dubonos, S.; Grigorieva, I. V.; Firsov, A. A. Electric field effect in atomically thin carbon films. *Science* **2004**, *306*, 666–669.
- (2) Wang, Q. H.; Kalantar-Zadeh, K.; Kis, A.; Coleman, J. N.; Strano, M. S. Electronics and optoelectronics of two-dimensional transition metal dichalcogenides. *Nat. Nanotechnol.* **2012**, *7*, 699–712.
- (3) Geim, A. K.; Grigorieva, I. V. Van der Waals heterostructures. *Nature* **2013**, *499*, 419–425.
- (4) Bonaccorso, F.; Sun, Z.; Hasan, T.; Ferrari, A. Graphene photonics and optoelectronics. *Nat. Photonics* **2010**, *4*, 611–622.
- (5) Bao, Q.; Loh, K. P. Graphene photonics, plasmonics, and broadband optoelectronic devices. *ACS Nano* **2012**, *6*, 3677–3694.
- (6) Grigorenko, A.; Polini, M.; Novoselov, K. Graphene plasmonics. *Nat. Photonics* **2012**, *6*, 749–758.
- (7) Iorsh, I. V.; Mukhin, I. S.; Shadrivov, I. V.; Belov, P. A.; Kivshar, Y. S. Hyperbolic metamaterials based on multilayer graphene structures. *Phys. Rev. B: Condens. Matter Mater. Phys.* **2013**, *87*, No. 075416.
- (8) Gomez-Diaz, J. S.; Tymchenko, M.; Alù, A. Hyperbolic plasmons and topological transitions over uniaxial metasurfaces. *Phys. Rev. Lett.* **2015**, *114*, No. 233901.
- (9) Lee, S. H.; Choi, M.; Kim, T.-T.; Lee, S.; Liu, M.; Yin, X.; Choi, H. K.; Lee, S. S.; Choi, C.-G.; Choi, S.-Y.; Zhang, X.; Min, B. Switching terahertz waves with gate-controlled active graphene metamaterials. *Nat. Mater.* **2012**, *11*, 936–941.
- (10) Fedorov, A. Viewpoint: The all-organic route to doping graphene. *Physics* **2010**, *3*, 46.
- (11) Cheng, J.; Wang, W. L.; Mosallaei, H.; Kaxiras, E. Surface plasmon engineering in graphene functionalized with organic molecules: A multiscale theoretical investigation. *Nano Lett.* **2014**, *14*, 50–56.
- (12) Wang, F.; Zhang, Y.; Tian, C.; Girit, C.; Zettl, A.; Crommie, M.; Shen, Y. R. Gate-variable optical transitions in graphene. *Science* **2008**, *320*, 206–209.
- (13) Zhang, Y.; Jiang, Z.; Small, J.; Purewal, M.; Tan, Y.-W.; Fazlollahi, M.; Chudow, J.; Jaszcza, J.; Stormer, H.; Kim, P. Landau-level splitting in graphene in high magnetic fields. *Phys. Rev. Lett.* **2006**, *96*, No. 136806.
- (14) Inampudi, S.; Nazari, M.; Forouzmand, A.; Mosallaei, H. Manipulation of surface plasmon polariton propagation on isotropic and anisotropic two-dimensional materials coupled to boron nitride heterostructures. *J. Appl. Phys.* **2016**, *119*, No. 025301.
- (15) Thongrattanasiri, S.; Manjavacas, A.; Garcia de Abajo, F. J. Quantum finite-size effects in graphene plasmons. *ACS Nano* **2012**, *6*, 1766–1775.
- (16) Xia, F.; Wang, H.; Xiao, D.; Dubey, M.; Ramasubramaniam, A. Two-dimensional material nanophotonics. *Nat. Photonics* **2014**, *8*, 899–907.
- (17) Majumdar, A.; Kim, J.; Vuckovic, J.; Wang, F. Electrical control of silicon photonic crystal cavity by graphene. *Nano Lett.* **2013**, *13*, S15–S18.
- (18) Ling, X.; et al. Parallel Stitching of 2D Materials. *Adv. Mater.* **2016**, *28*, 2322–2329.
- (19) Elser, J.; Podolskiy, V. A. Scattering-free plasmonic optics with anisotropic metamaterials. *Phys. Rev. Lett.* **2008**, *100*, No. 066402.
- (20) Yu, N.; Genevet, P.; Kats, M. A.; Aieta, F.; Tetienne, J.-P.; Capasso, F.; Gaburro, Z. Light propagation with phase discontinuities: generalized laws of reflection and refraction. *Science* **2011**, *334*, 333–337.
- (21) Foley, J. J., IV; McMahon, J. M.; Schatz, G. C.; Harutyunyan, H.; Wiederrecht, G. P.; Gray, S. K. Inhomogeneous Surface Plasmon Polaritons. *ACS Photonics* **2014**, *1*, 739–745.
- (22) Lezec, H. J.; Dionne, J. A.; Atwater, H. A. Negative refraction at visible frequencies. *Science* **2007**, *316*, 430–432.
- (23) Garcia-Pomar, J. L.; Nikitin, A. Y.; Martin-Moreno, L. Scattering of graphene plasmons by defects in the graphene sheet. *ACS Nano* **2013**, *7*, 4988–4994.
- (24) Nikitin, A. Y.; López-Tejeira, F.; Martín-Moreno, L. Scattering of surface plasmon polaritons by one-dimensional inhomogeneities. *Phys. Rev. B: Condens. Matter Mater. Phys.* **2007**, *75*, No. 035129.
- (25) Kumar, A.; Fung, K. H.; Reid, M. H.; Fang, N. X. Transformation optics scheme for two-dimensional materials. *Opt. Lett.* **2014**, *39*, 2113–2116.
- (26) Woessner, A.; Lundeberg, M. B.; Gao, Y.; Principi, A.; Alonso-González, P.; Carrega, M.; Watanabe, K.; Taniguchi, T.; Vignale, G.; Polini, M.; Hone, J.; Hillenbrand, R.; Koppens, F. H. Highly confined low-loss plasmons in graphene-boron nitride heterostructures. *Nat. Mater.* **2015**, *14*, 421–425.
- (27) Efetov, D. K.; Kim, P. Controlling electron-phonon interactions in graphene at ultrahigh carrier densities. *Phys. Rev. Lett.* **2010**, *105*, No. 256805.
- (28) Thongrattanasiri, S.; Elser, J.; Podolskiy, V. A. Quasi-planar optics: computing light propagation and scattering in planar waveguide arrays. *J. Opt. Soc. Am. B* **2009**, *26*, B102–B110.
- (29) Inampudi, S.; Smolyaninov, I. I.; Podolskiy, V. A. Low-diffraction beaming in plasmonic crystals. *Opt. Lett.* **2012**, *37*, 2976–2978.
- (30) Shirodkar, S. N.; Kaxiras, E. Li intercalation at graphene/hexagonal boron nitride interfaces. *Phys. Rev. B* **2016**, *93*, No. 245438.
- (31) Jang, C.; Adam, S.; Chen, J.-H.; Williams, E.; Sarma, S. D.; Fuhrer, M. Tuning the effective fine structure constant in graphene: opposing effects of dielectric screening on short-and long-range potential scattering. *Phys. Rev. Lett.* **2008**, *101*, No. 146805.
- (32) Joannopoulos, J. D.; Johnson, S. G.; Winn, J. N.; Meade, R. D. *Photonic Crystals: Molding the Flow of Light*; Princeton University Press, 2011.
- (33) Mao, S.; Yu, K.; Chang, J.; Steeber, D. A.; Ocola, L. E.; Chen, J. Direct growth of vertically-oriented graphene for field-effect transistor biosensor. *Sci. Rep.* **2013**, *3*, No. 1696.
- (34) Geng, W.; Ping, D.; Nara, J.; Ohno, T. Formation of perpendicular graphene nanosheets on LiFePO<sub>4</sub>: A first-principles characterization. *J. Phys. Chem. C* **2012**, *116*, 17650–17656.
- (35) Yu, J. H.; Lee, H. R.; Hong, S. S.; Kong, D.; Lee, H.-W.; Wang, H.; Xiong, F.; Wang, S.; Cui, Y. Vertical heterostructure of two-dimensional MoS<sub>2</sub> and WSe<sub>2</sub> with vertically aligned layers. *Nano Lett.* **2015**, *15*, 1031–1035.
- (36) Moharam, M.; Gaylord, T.; Grann, E. B.; Pommet, D. A. Formulation for stable and efficient implementation of the rigorous coupled-wave analysis of binary gratings. *J. Opt. Soc. Am. A* **1995**, *12*, 1068–1076.
- (37) Yu, N.; Capasso, F. Optical metasurfaces and prospect of their applications including fiber optics. *J. Lightwave Technol.* **2015**, *33*, 2344–2358.
- (38) Farmahini-Farahani, M.; Cheng, J.; Mosallaei, H. Metasurfaces nanoantennas for light processing. *J. Opt. Soc. Am. B* **2013**, *30*, 2365–2370.
- (39) Cheng, J.; Mosallaei, H. Optical metasurfaces for beam scanning in space. *Opt. Lett.* **2014**, *39*, 2719–2722.
- (40) Cheng, J.; Ansari-Oghol-Beig, D.; Mosallaei, H. Wave manipulation with designer dielectric metasurfaces. *Opt. Lett.* **2014**, *39*, 6285–6288.

- (41) Yu, N.; Capasso, F. Flat optics with designer metasurfaces. *Nat. Mater.* **2014**, *13*, 139–150.
- (42) Li, Z.; Yao, K.; Xia, F.; Shen, S.; Tian, J.; Liu, Y. Graphene Plasmonic Metasurfaces to Steer Infrared Light. *Sci. Rep.* **2015**, *5*, No. 12423.
- (43) Sun, S.; Yang, K.-Y.; Wang, C.-M.; Juan, T.-K.; Chen, W. T.; Liao, C. Y.; He, Q.; Xiao, S.; Kung, W.-T.; Guo, G.-Y.; Zhou, L.; Tsai, D. P. High-efficiency broadband anomalous reflection by gradient meta-surfaces. *Nano Lett.* **2012**, *12*, 6223–6229.
- (44) Kildishev, A. V.; Boltasseva, A.; Shalaev, V. M. Planar photonics with metasurfaces. *Science* **2013**, *339*, No. 1232009.
- (45) Satuby, Y.; Orenstein, M. Surface-Plasmon-Polariton modes in deep metallic trenches-measurement and analysis. *Opt. Express* **2007**, *15*, 4247–4252.
- (46) Feigenbaum, E.; Orenstein, M. Modeling of complementary (void) plasmon waveguiding. *J. Lightwave Technol.* **2007**, *25*, 2547–2562.
- (47) Pile, D. F.; Gramotnev, D. K.; Oulton, R. F.; Zhang, X. On long-range plasmonic modes in metallic gaps. *Opt. Express* **2007**, *15*, 13669–13674.